Natural radio emission of Jupiter as interferences for radar investigations of the icy satellites of Jupiter

B. Cecconi[a], S. Hess[b], A. Hérique[c], M.R. Santovito[d], D. Santos-Costa[e], P. Zarka[a], G. Alberti[d], D. Blankenship[f], J.-L. Bougeret[a], L. Bruzzone[g], W. Kofman[c]

[a]*LESIA, CNRS-Observatoire de Paris, Meudon, France*
[b]*LASP, University of Colorado at Boulder, USA*
[c]*LPG,CNRS-Université Joseph Fourier Grenoble, France*
[d]*CO.RI.S.T.A., Naples, Italy*
[e]*Space Science Department, Southwest Research Institute, Texas, USA*
[f]*Institute of Geophysics, University of Texas at Austin, USA*
[g]*Department of Civil and Environment Engineering, University of Trento, Italy*

Abstract

Radar instruments are part of the core payload of the two Europa Jupiter System Mission (EJSM) spacecraft: NASA-led Jupiter Europa Orbiter (JEO) and ESA-led Jupiter Ganymede Orbiter (JGO). At this point of the project, several frequency bands are foreseen for radar studies between 5MHz and 50MHz. While the high frequencies (above ∼40 MHz) are clean bands since natural jovian radio emissions show a high frequency cutoff at about 40 MHz, lower frequencies are right in the middle of the intense decametric (DAM) radio emissions. We present a review of spectral intensity, variability and sources of these radio emissions. As the radio emission are strongly beamed, it is possible to model the visibility of the radio emissions, as seen from the vicinity of Europa or Ganymede. We have investigated Io-related radio emissions as well as radio emissions related to the auroral oval. We also review the radiation belts synchrotron emission characteristics. We present radio sources visibility products (dynamic spectra and radio source location maps, on still frames or movies), that can be used for operation planning. This study clearly shows that a deep understanding of the natural radio emissions at Jupiter is necessary to prepare the future EJSM radar instrumentation. We show that this radio noise has to be taken into account very early in the observation planning and strategies for both JGO and JEO. We also support strong synergies with RPW (Radio and Plasma Waves) instrumentations.

Keywords: Jupiter; EJSM/Laplace; Radio emissions; Galilean satellites; Radar instrumentation.

1. Introduction

In the frame of the future ESA-NASA EJSM (Europa Jupiter System Mission), currently in competition with two other missions, instrumental studies have been initiated by ESA to evaluate the technical feasibility and science objectives of the different instrumental packages. The EJSM/Laplace concept is composed of two spacecraft: NASA-led JEO (Jupiter Europa Orbiter) and ESA-led JGO (Jupiter Ganymede Orbiter). The study of subsurface layers of Europa and Ganymede is one of the first science objectives of this space mission. Unfortunately, the radio environment of Jupiter is dominated by strong natural radio emissions, which will interfere with radar measurements near Europa or Ganymede.

The jovian radio emissions were discovered by Burke and Franklin (1955). Since then, decades of ground based and space based observations provided a good knowledge of the characteristics of these emissions. Ground based observations are limited by the terrestrial ionospheric cutoff, which reflects out radio waves with frequencies lower than 10 MHz. Space based observations are usually limited at high frequencies because of the limited resources available on a spacecraft. As reviewed by Zarka (1998) and recalled on Figs. 1 and 2, the jovian radio spectrum is composed of several components that will be reviewed in this paper. These radio emissions dominates the galactic background Cane (1979), which is usually the only source of noise for planetary radar measurements.

The radar instrumentation that is developed for the EJSM mission is foreseen to operate at frequencies ranging between 5 MHz to 50 MHz. This frequency range can be split into two ranges at ∼40 MHz. Below that limit, the radio spectrum is dominated by very intense and sporadic cyclotron radio emissions with sources located along high latitude field lines, close to Jupiter. At higher frequencies, the radio noise will be the combination of the galactic background and the synchrotron radiation emitted by the jovian radiation belts.

In this paper, we will first review the different natural sources of radio interferences. In a second section, the flux

Email address: baptiste.cecconi@obspm.fr (B. Cecconi)

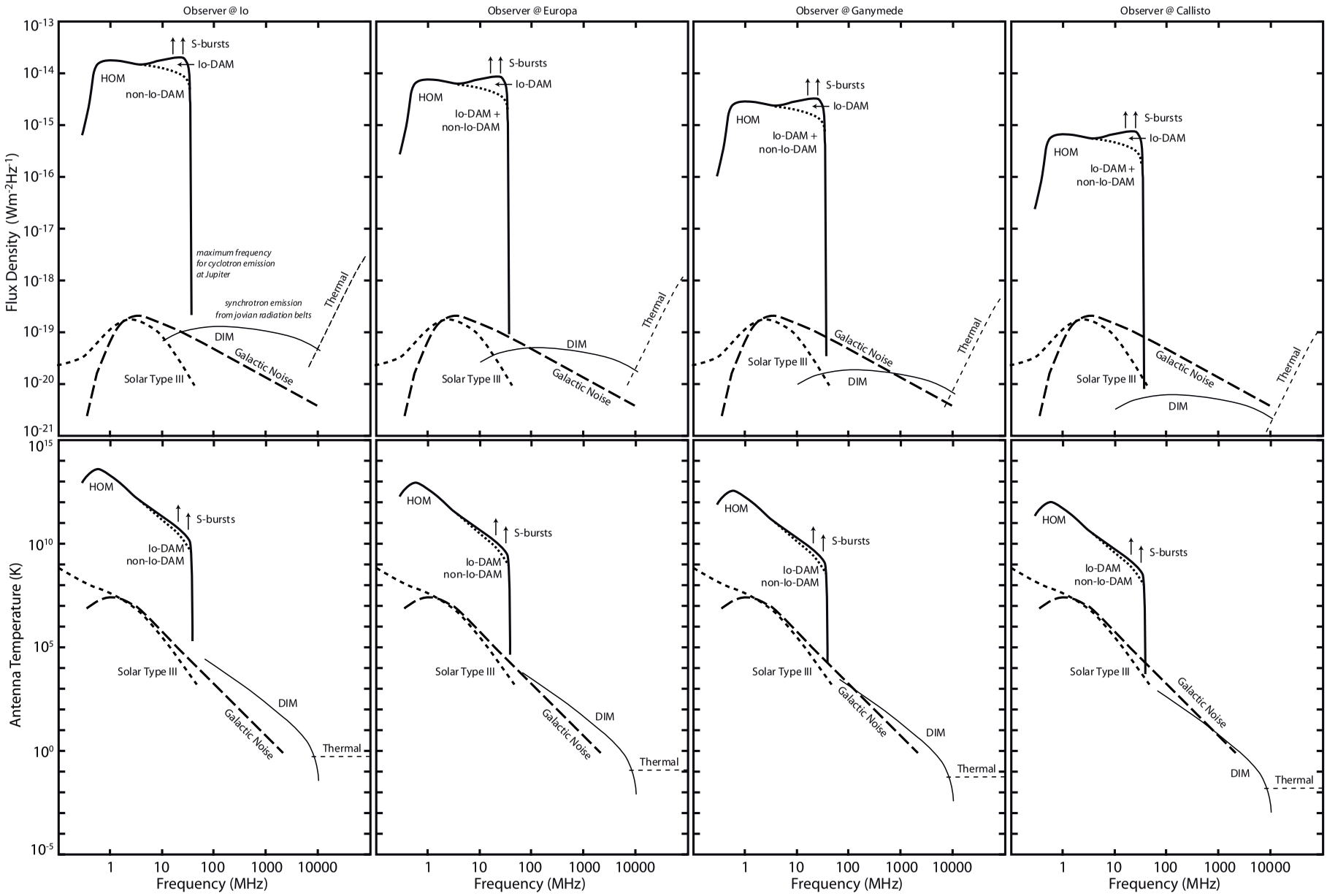

Figure 1: Spectral Flux Density (top row) and Antenna Temperature (bottom row) of the radio emissions at Jupiter in units of $Wm^{-2}Hz^{-1}$ (top) and K (bottom). See Appendix A for conversions between these quantities. *HOM*: Hectometric Radiation; *S-bursts*: Short (or Millisecond) Bursts; *Io-DAM*: Io-controlled Decametric Radiation; *non-Io-DAM*: non-Io-controlled Decametric Radiation; *DIM*: Decimetric Radiation (synchrotron emission from radiation belts); *Thermal*: Black body thermal radiation; *Solar Type III*: solar type III radio bursts; *Galactic Noise*: Galactic background radiation. Figure Adapted from Zarka (1992), updated with Zarka et al. (2004); Zarka (2007)

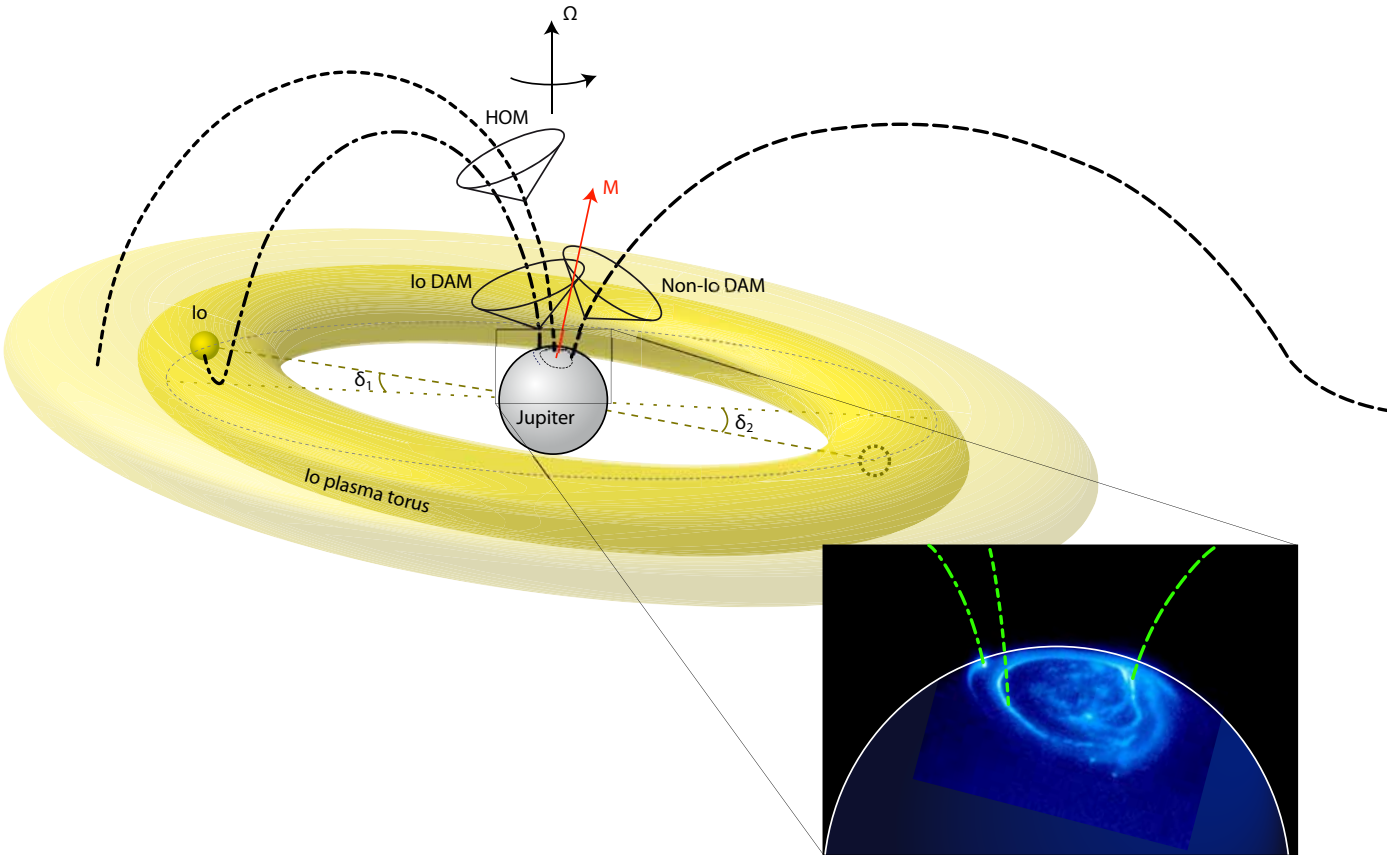

Figure 2: High latitude jovian radio sources. The radio emissions are emitted by relativistic electrons precipitating and bouncing out along magnetic field lines, in the jovian auroral regions. These electrons are accelerated near the magnetic field apex: in the plasma wake of Io for Io-DAM emissions, or in the plasma disk for Non-Io-DAM and HOM emissions. The radio emission pattern is not isotropic. They waves are emitted along a thin hollow cone represented on the figure. For instance, Io-DAM emissions are only visible when the emission cone is illuminating the observer. Note that there is a longitudinal lag between the magnetic longitude of Io and that of the Io-controlled radio sources. This angle is usually called the lead angle. It depends on the magnetic longitude of Io, because the sidereal and magnetic axis of Jupiter are not aligned, and on the observer location. This angle represented for the two phases of Io when the emission is visible (δ_1 and δ_2).

density of these radio waves is compared to the predicted signal strength of radar soundings at the different jovian icy satellites. We present then visibility modeling of radio sources, inferring time intervals and frequency ranges clean from natural radio emissions. We will also discuss various ways to mitigate the natural radio emissions. We finally discuss the results of the study and conclude.

2. Overview of jovian radio environment

Fig. 1 shows the radio emission spectra that are visible near Jupiter. In the frequency range of interest for radar studies (5 to 50 MHz), the radio components can be separated into four categories: (i) non-thermal jovian radio emissions emitted on high latitude magnetic field lines (Io-DAM, non-Io-DAM and S-bursts), (ii) synchrotron radiation from the jovian radiation belts (DIM); (iii) solar radio emissions (Solar Type III bursts); and (iv) the galactic background emission. Refer to the caption of Fig. 1 for the abbreviations of the component names. We will review here each of these components.

2.1. High latitude radio emissions

The high latitude Jovian radio emissions are emitted in the decametric range of frequency (from ∼3 MHz to ∼40 MHz). These frequencies correspond to the local electron cyclotron frequencies (f_{ce}) along the magnetic field lines between the top of the Jovian ionosphere and the border of the equatorial Io plasma torus. The electron cyclotron frequency f_{ce} relates to the local magnetic field B via $f_{ce} = q_e B/2\pi m_e$, with q_e the charge of an electron, m_e its mass. Hence, the higher frequencies are emitted closer to the planet.

These radio emissions are presumably emitted by a non linear wave-particle interaction called the Cyclotron Maser Instability (CMI) (Wu and Lee, 1979; Treumann, 2006). This mechanism involves the resonance between the gyromotion of the electron and a circularly polarized wave. The direction of the electron gyromotion depending on the direction of the magnetic field, emissions from opposite hemispheres have opposite polarizations. At Jupiter, emissions from the northern (resp. southern) hemisphere are right-handed (resp. left-handed) polarized.

The CMI needs high energy electrons (∼0.1c), and an unstable electron distribution function. Such distributions are produced in acceleration processes that occur in various regions of the magnetosphere of Jupiter, such as the current systems induced by the interactions of the Jovian magnetosphere with Io, feeding the Io-DAM emissions; or the plasma disk, feeding the non-Io-DAM emissions (see Fig. 2).

2.1.1. Spectral shape and occurrence

The spectral shape the auroral radio sources is given on the top row of Fig. 1. The peak flux density is of the order of $10^{-14}\,Wm^2/Hz$ between 5 and 40 *MHz*. The spectrum shows a very steep cut off at ∼40 *MHz*. This high frequency cutoff corresponds to f_{ce} right above the ionosphere of Jupiter. In the frame of the CMI, no radio waves can be emitted at higher frequencies than ∼40 MHz at Jupiter.

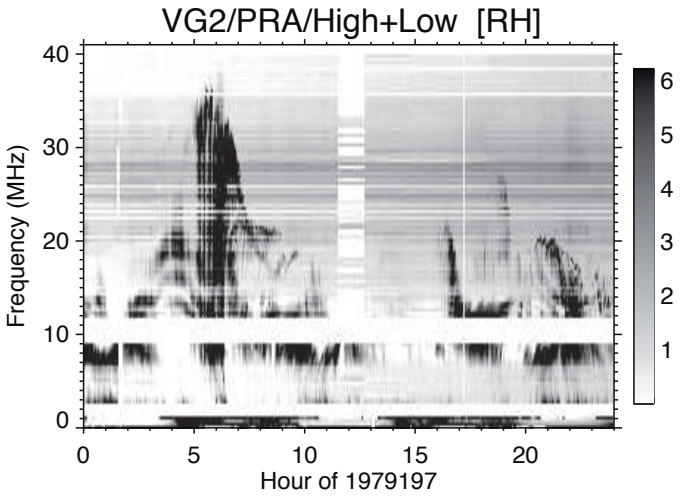

Figure 3: Dynamic Spectrum of the jovian radio emissions observed by the PRA (Planetary Radio Astronomy) instrument onboard the Voyager-2 spacecraft, on day 1979-197 (July 16th). The plot includes data from High Band and Low Band receivers, with right hand (RH) polarization selection. This figure shows a typical example of Io-DAM emission (black stripes that goes from ∼5 MHz to 35 MHz, between 06:00 and 10:00).

These emissions are also very sporadic and are showing arc-like features in the time-frequency domain (see Fig. 3). These shapes can be interpreted as a geometrical effect: The radio emissions have a very anisotropic beaming pattern, so that even if the emission is continuous, it can only be observed when the observer is in the direction of emission. In the case of the Io-related emissions, the longitude of the emissions (close to Io's longitude) and the beaming pattern are strongly constrained. Thus the occurrence of the Io-DAM emissions can be predicted. Although Non-Io-DAM emissions show a similar beaming pattern, the longitude at which they occur is variable. Hence their temporal occurrence can only be predicted in a probabilistic manner.

2.1.2. Radio Wave Polarization

The radio waves in the decametric range are observed with elliptical polarization from Earth (Lecacheux, 1988; Lecacheux et al., 1991). In the hectometric range, Ulysses radio observations showed circular polarization close to the equatorial plane (±30° from the equator), and elliptical polarization at high latitudes (Reiner et al., 1995). The presence of elliptical polarization in these radio emission is still under study and is one of the science objectives of RPW (Radio and Plasma Waves) instrumentation for EJSM. The polarization of the waves have a direct incidence on the power received by an electric dipole (see Appendix A).

2.1.3. Beaming

A key aspect of these radio emissions is that they are strongly beamed. Their observed emission beaming pattern is a thin (1°) conical sheet (Ellis, 1982) with a large opening angle ($\sim 70°$ to $90°$), whose axis is aligned with the magnetic field vector in the source. The direction of emission, i.e. opening angle of the beaming hollow cone, is dictated by the distribution function of the electrons, and by the plasma density profile close to the source. In the Jovian case, the refraction effects due to the density are negligible almost everywhere, so that knowing the distribution function of the electrons permits to get an accurate approximation of the beaming angle.

The beaming angle profile versus the emission frequency has been studied for Io-DAM (Queinnec and Zarka, 1998; Hess et al., 2008; Ray and Hess, 2008) and non-Io-DAM (Imai et al., 2008), allowing for accurate modeling of the visibility of the radio emission, as discussed in section 4.

It has notably been shown that, due to the large beaming angle of the emissions, they can only been seen when the sources are close to the limb of Jupiter. Hence the emissions have been divided into four ranges: the A and C ranges, which corresponds to sources observed with a $\sim 270°$ phase, from the northern and southern hemisphere respectively, and the B and D ranges, corresponding to sources observed with a $\sim 90°$ phase from the northern and southern hemisphere.

2.1.4. Fine Structures

The Io-controlled radio emissions are characterized by very intense fine structures drifting in frequencies, called S-bursts, or millisecond bursts. S-bursts are observed from ground based radio telescopes with high frequency and temporal resolution (Ryabov et al., 2007).

The S-bursts usually show negative frequency drifts between -15 and $-25 MHz/s$ (Zarka et al., 1996). Successive S-bursts are separated by a few tens of milliseconds. As shown on Fig. 1 of Ryabov et al. (2007), S-bursts are not always behaving with a clean negative frequency drift. However, observing consistent positive frequency drifts in S-bursts is rather unlikely.

The drift of these emissions corresponds to the motion of keV electrons along the magnetic field lines. These electrons are accelerated by the same current systems that generate the Io-DAM radio arcs. Thus they occur usually few minutes before, or after, the radio arcs. It implies that the occurrence of the S-bursts storms can be predicted in the same way than that of the Io-related radio arcs.

2.2. Jovian lightning induced radio emissions

No radio emission from lightning in the range from MHz to tens of MHz was detected at Jupiter, by any visiting spacecraft (Voyagers, Galileo, and Cassini), except for the search coil on the Galileo descent probe which recorded below the ionosphere signals attributed to lightning up to 90 kHz (Lanzerotti et al., 1996), although we have strong evidence for the presence of lightning there: optical ashes were observed by Voyager, Galileo, and Cassini, and low-frequency whistlers were detected by the two Voyager spacecraft (see Cook II et al., 1979; Gurnett et al., 1979; Desch et al., 2002, and references therein).

In addition to masking of hypothetic lightning signal by the intense decameter radiation from Jupiter's magnetosphere, two explanations have been proposed for the non-detection of Jovian lightning in the radio range (see Zarka et al., 2004, and references therein):

- Zarka (1985) demonstrated that the low-altitude ionospheric layers discovered by Pioneer 10 and 11 would cause very strong absorption (several tens of dB attenuation) of radio waves generated in the atmosphere. These low-altitude ionospheric layers, with electron concentrations above $10^5\ cm^{-3}$ at an altitude of a few hundred km above the 1 bar level, possibly have a (micro-)meteoritic origin;

- Farrell et al. (1999) conversely proposed, on the basis of electric field measurements performed in Jupiter's atmosphere by Galileo's descent probe, that Jovian lightning discharges could have much longer time constants than their Terrestrial or Saturnian counterparts: a rise time of a few milliseconds at Jupiter versus tens of microseconds (Earth) to tens of nanoseconds (Saturn). The reason for these possibly "slow" lightning strokes at Jupiter is not known. They would imply radio emission spectra restricted to very low frequencies, well below Jupiter's ionospheric cutoff frequency. Similar slow rise times have been observed for Terrestrial cloud-to-ionosphere discharges (sprites: Sentman et al., 1995).

2.3. Solar radio bursts

Solar type III bursts are the most intense radio emissions emitted by the Sun in the studied frequency range. These bursts are radiated by relativistic electron beams emitted by active regions on the Sun. These bursts are lasting a few seconds at 20 MHz and their mean flux density is comparable with the galactic background. However, these bursts show a wide range of intensity (Weber, 1978; Bonnin, 2008), partially due to their beaming properties, so they can be one order of magnitude stronger than represented on Fig. 1.

2.4. Synchrotron emission

The Jovian radiation belts are producing synchrotron radio emissions in the metric and decimetric range (from $\sim$40 MHz to $\sim$10 GHz). This component of the Jovian radio spectrum has been reviewed by (de Pater, 2004).

Figure 4 depicts the first simulated radio spectrum of Jupiter's non-thermal microwave emission for the [0.01; 15] GHz frequency range. The computed profile was verified with measurements made at frequencies above 0.1 GHz and at different epochs. Radio data show fluctuations in

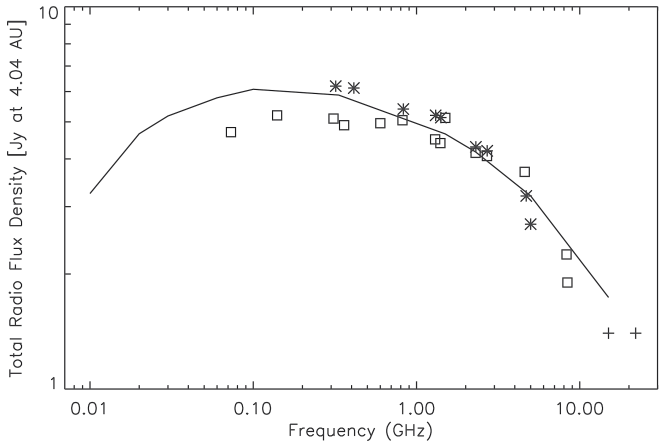

Figure 4: Radio spectrum of Jupiter's synchrotron radiation in the [0.01; 15] GHz frequency range. The simulated spectrum (solid line) was computed by combining a synchrotron simulation code with a particle diffusion transport model (e.g., Santos-Costa and Bolton, 2008). The cross symbols represent data taken in March 1991, star symbols for data collected in June 1994, and observations in September 1998 were plotted using the square symbols (e.g., de Pater and Dunn, 2003)

the total flux density with time and frequency within a factor 2. Origins of the observed variations are associated with changes in the spatial and energy distributions of the energetic electrons trapped in Jupiter's magnetosphere. The dynamical behavior of the Jovian electron belt has been linked to solar activity to explain the long-term variability of Jupiter's synchrotron emission (e.g., de Pater and Dunn, 2003; Santos-Costa and Bolton, 2008). The profile for the whole radio band was computed by combined a synchrotron simulation code with a particle diffusion transport code (Santos-Costa, 2001). For each of the ten frequencies picked-up in the frequency range [0.007; 15] GHz, the total flux density was deduced from the mean value of the beaming curve (i.e., longitude-average of the modulation of the total flux density with Jupiter rotation). Each beaming curve was built from eighteen two-dimensional simulated brightness distributions of the Jovian synchrotron radio emission. All calculations were made for a distance of 4.04 AU and setting the geometrical parameter D_E (Earth declination as seen from Jupiter) to zero degree.

2.5. Galactic background

The radio spectrum of the galactic background radiation (resulting from the free-free interactions of the electrons in the galactic magnetic field) has been studied by either ground based or space borne observers (Novaco and Brown, 1978; Cane, 1979). This spectrum has been modeled by Dulk et al. (2001); Manning and Dulk (2001) in the 1–100 MHz range. This model has been used for the curves plotted on Fig. 1.

3. Comparison with radar echoes

As described in the previous Section, the natural radio noise at Jupiter is a complex combination of high intensity radio signals varying on a large range of timescales (from milliseconds to hours). It is thus important to correctly estimate the signal strength of the radar echoes compared to the ambient radio noise. We will consider realistic parameters for the radar transmitter and receiver characteristics, as well as for the Galilean satellites ice properties. These operational values are given in Table 1 and are adapted from Kofman et al. (2010), and corresponds to JGO-like radar instrumentation. We also discuss JEO-like radar instrumentation at the end of this section.

3.1. Radar echo strength

According to monostatic Radar equation (Kofman et al., 2010), the received signal strength P_{RX} is:

$$\mathcal{P}_{RX} = \frac{\mathcal{P}_{TX}\lambda^2 G^2 \tau_p b (1-|r_{surface}|^2) r_{layer}^2 10^{-\alpha z/10} L_{sys}}{(4\pi)^2 (2(R+z))^2} \quad (1)$$

with $\mathcal{P}_{TX}$ the transmitted signal power, λ the transmitting wavelength, G the antenna gain, $r_{surface}$ the effective reflectivity of the ice-atmosphere interface, r_{layer} the effective reflectivity of an internal layer, α the 2-way attenuation through ice of thickness z, L_{sys} system losses including internal transmission losses and losses within the antenna during transmission, R range from satellite to ice surface, z depth from the surface to the internal layer, τ_p the pulse duration and b the bandwidth of transmitted pulse. Operating parameters to be used to compute numerical values of the back scattered signal power are provided in Table 1. The effective reflectivity values have evaluated from the permittivities of the various layers, as follows:

$$r_{12} = \frac{\sqrt{\varepsilon_1} - \sqrt{\varepsilon_2}}{\sqrt{\varepsilon_1} + \sqrt{\varepsilon_2}}. \quad (2)$$

The $|r_{surface}| = 0.27$ value is obtained with $\varepsilon_{atm} = 1$ and $\varepsilon_{surface} = 3$. The $|r_{layer}| \sim 0.21$ to 0.68 range is obtained with two possible values for the subsurface layer permittivity: $\varepsilon_{layer} = 7$ for a layer composed of basalt and $\varepsilon_{layer} = 80$ for a liquid ocean layer. The proposed formula do not include diffusion effects due the surface roughness. Including these effects would reduce the observed echo signals.

With these numbers, we can estimate power of the echo signal scattered back to the antenna $\mathcal{P}_{RX}$. The received power can be converted into spectral flux density with:

$$S_{RX} = \frac{8\pi}{3\lambda^2}\frac{\mathcal{P}_{RX}}{b} \quad (3)$$

which does not depend on wavelength, as $\mathcal{P}_{RX}$ already contains a λ^2 factor. This also converts into antenna temperature as follows:

$$T_A = \frac{\mathcal{P}_{RX}}{k_B b} \quad (4)$$

Numerical values are presented in Table 2 and shall be compared to the spectra shown on Fig. 1.

Parameters				Antenna Temperature (short antenna: $G = 3/2$) (K)				Antenna Temperature (adapted antenna: $G = 3.3$) (K)			
R (km)	z (km)	α (dB/km)	r_{layer}	20 MHz	30 MHz	40 MHz	50 MHz	20 MHz	30 MHz	40 MHz	50 MHz
200	1	5	0.2	2.18×10^7	9.67×10^6	5.44×10^6	$\mathbf{3.48 \times 10^6}$	1.05×10^8	4.68×10^7	2.63×10^7	$\mathbf{1.68 \times 10^7}$
200	1	5	0.1	5.44×10^6	2.42×10^6	1.36×10^6	$\mathbf{8.70 \times 10^5}$	2.63×10^7	1.17×10^7	6.58×10^6	$\mathbf{4.21 \times 10^6}$
200	1	10	0.2	6.88×10^6	3.06×10^6	1.72×10^6	$\mathbf{1.10 \times 10^6}$	3.33×10^7	1.48×10^7	8.32×10^6	$\mathbf{5.33 \times 10^6}$
200	1	10	0.1	1.72×10^6	7.64×10^5	4.30×10^5	$\mathbf{2.75 \times 10^5}$	8.32×10^6	3.70×10^6	2.08×10^6	$\mathbf{1.33 \times 10^6}$
200	2	5	0.2	6.81×10^6	3.03×10^6	1.70×10^6	$\mathbf{1.09 \times 10^6}$	3.30×10^7	1.47×10^7	8.24×10^6	$\mathbf{5.27 \times 10^6}$
200	2	5	0.1	1.70×10^6	7.57×10^5	4.26×10^5	$\mathbf{2.72 \times 10^5}$	8.24×10^6	3.66×10^6	2.06×10^6	$\mathbf{1.32 \times 10^6}$
200	2	10	0.2	6.81×10^5	3.03×10^5	1.70×10^5	$\mathbf{1.09 \times 10^5}$	3.30×10^6	1.47×10^6	8.24×10^5	$\mathbf{5.27 \times 10^5}$
200	2	10	0.1	1.70×10^5	7.57×10^4	4.26×10^4	$\mathbf{2.72 \times 10^4}$	8.24×10^5	3.66×10^5	2.06×10^5	$\mathbf{1.32 \times 10^5}$
200	5	5	0.2	2.09×10^5	9.29×10^4	5.23×10^4	$\mathbf{3.35 \times 10^4}$	1.01×10^6	4.50×10^5	2.53×10^5	$\mathbf{1.62 \times 10^5}$
200	5	5	0.1	5.23×10^4	2.32×10^4	1.31×10^4	8.36×10^3	2.53×10^5	1.12×10^5	6.33×10^4	$\mathbf{4.05 \times 10^4}$
200	5	10	0.2	6.61×10^2	2.94×10^2	1.65×10^2	1.06×10^2	3.20×10^3	1.42×10^3	8.00×10^2	5.12×10^2
200	5	10	0.1	1.65×10^2	7.35×10^1	4.13×10^1	2.65×10^1	8.00×10^2	3.56×10^2	2.00×10^2	1.28×10^2
500	1	5	0.2	3.50×10^6	1.56×10^6	8.75×10^5	$\mathbf{5.60 \times 10^5}$	1.69×10^7	7.53×10^6	4.24×10^6	$\mathbf{2.71 \times 10^6}$
500	1	5	0.1	8.75×10^5	3.89×10^5	2.19×10^5	$\mathbf{1.40 \times 10^5}$	4.24×10^6	1.88×10^6	1.06×10^6	$\mathbf{6.78 \times 10^5}$
500	1	10	0.2	1.11×10^6	4.92×10^5	2.77×10^5	$\mathbf{1.77 \times 10^5}$	5.36×10^6	2.38×10^6	1.34×10^6	$\mathbf{8.57 \times 10^5}$
500	1	10	0.1	2.77×10^5	1.23×10^5	6.92×10^4	$\mathbf{4.43 \times 10^4}$	1.34×10^6	5.95×10^5	3.35×10^5	$\mathbf{2.14 \times 10^5}$
500	2	5	0.2	1.10×10^6	4.90×10^5	2.76×10^5	$\mathbf{1.76 \times 10^5}$	5.34×10^6	2.37×10^6	1.33×10^6	$\mathbf{8.54 \times 10^5}$
500	2	5	0.1	2.76×10^5	1.23×10^5	6.89×10^4	$\mathbf{4.41 \times 10^4}$	1.33×10^6	5.93×10^5	3.34×10^5	$\mathbf{2.13 \times 10^5}$
500	2	10	0.2	1.10×10^5	4.90×10^4	2.76×10^4	$\mathbf{1.76 \times 10^4}$	5.34×10^5	2.37×10^5	1.33×10^5	$\mathbf{8.54 \times 10^4}$
500	2	10	0.1	2.76×10^4	1.23×10^4	6.89×10^3	4.41×10^3	1.33×10^5	5.93×10^4	3.34×10^4	$\mathbf{2.13 \times 10^4}$
500	5	5	0.2	3.45×10^4	1.53×10^4	8.61×10^3	5.51×10^3	1.67×10^5	7.41×10^4	4.17×10^4	$\mathbf{2.67 \times 10^4}$
500	5	5	0.1	8.61×10^3	3.83×10^3	2.15×10^3	1.38×10^3	4.17×10^4	1.85×10^4	1.04×10^4	6.67×10^3
500	5	10	0.2	1.09×10^2	4.84×10^1	2.72×10^1	1.74×10^1	5.27×10^2	2.34×10^2	1.32×10^2	8.44×10^1
500	5	10	0.1	2.72×10^1	1.21×10^1	6.81×10^0	4.36×10^0	1.32×10^2	5.86×10^1	3.30×10^1	2.11×10^1

Table 2: Numerical values of the echo signal strength evaluated from Eq. 1. Italic (resp. bold) figures indicate cases where echo signals are sometimes (resp. always) above the natural radio noise at Jupiter. Regular figures are always below the background level.

Parameter	Value(s)
$\mathcal{P}_{TX}$	$20\,W$
ν	20 to 50 MHz
L_D	5 to 10 m
λ	c/ν
G	1.5 ($L_D \ll \lambda$) up to ∼3.3 ($L_D = 1.26\lambda$)
τ_p	$150\,\mu s$
b	$10\,MHz$
$\|r_{surface}\|$	~ 0.27
$\|r_{layer}\|$	~ 0.21 to 0.68
α	~ 6 to 16 dB/km
L_{sys}	0.5
R	200 to 500 km
z	up to 5 km

Table 1: Numerical parameters for estimation of icy satellites radar measurements. L_D is the radar dipole length; ν is the operating frequency; see text for other parameters.

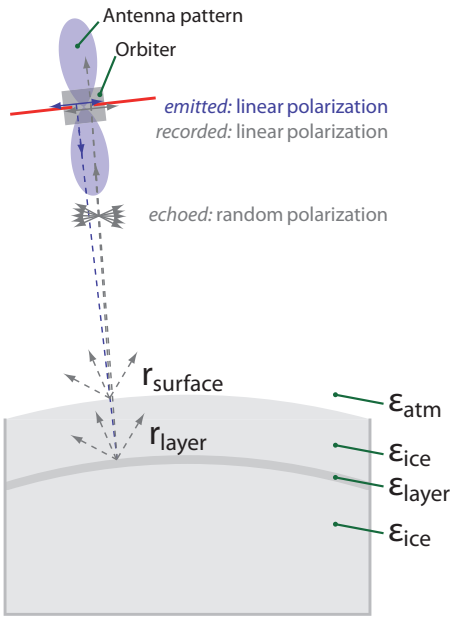

Figure 5: Radar pulse emission, reflection and reception. The radar instrument emits a radio pulse. This pulse is linearly polarized due to the geometry of the antenna. The surface and subsurface layers are reflecting the pulse. Depending on the properties of the surface and layer interfaces, the echoes have various intensity and various polarization properties. In our case, the up-going echo is randomly polarized. As the radar antenna is a dipole, it can sense only linear polarization. The received signal is thus a fraction of the echoed pulses.

3.2. Radar chirp signal

In order to enhance the signal mitigation, modern radar instrumentation use chirped input signals. These signals are brief power pulses quickly drifting in frequency. This described in several studies (see, e.g., Djurík and Kay, 1990; Picardi et al., 1999, 2004; Seu et al., 2004). The chirp is usually generated using a voltage control oscillator (e.g., sweeping from 1 to 10 MHz), and then translated to higher frequencies using heterodyne mixers.

Using the numbers given in Table 1, we get a drift rate of ∼67 GHz/s, which is much higher than the observed drift rates of the S-bursts, which are of the order of ∼10 MHz/s. The S-bursts are then expected to appear as constant fixed-frequency lines during the time of a chirp.

3.3. Dipole versus Yagi antennas

The type of antenna studied for JGO and JEO are different. On JGO, the radar team plans to use a dipole antenna as described on Fig. 5, whereas the JEO team is studying a Yagi antenna design (Blankenship et al., 1999). The JGO dipole antenna gains for various operating and antenna lengths are shown on Fig. 6. The Yagi antenna designed for JEO is illustrated on Fig. 7, where the bottom panel shows the antenna design, and the top panel the antenna emission pattern in the cross-track plane (bold line) and along-track plane (thin line). Comparing the two figures, we conclude that: (ii) the antenna pattern of a dipole antenna shows a single main lobe perpendicular to the antenna direction only for low frequencies; (ii) at higher frequencies, the dipole antenna pattern is multilobed; (iii) the main lobe of a Yagi antenna is pointed towards the front direction (observing direction); (iv) the gain of a Yagi antenna is very small in the back direction (opposite to the observing direction), which is not the case for a dipole antenna, which has the same gain in the front and back directions; (v) the dipole antenna pattern has a null in the antenna direction, whereas the Yagi antenna does not.

4. Radio emission visibility modeling

4.1. Modeling tool

The ExPRES (Exoplanetary and Planetary Radio Emissions Simulator) (Hess et al., 2008) allows us to predict the CMI induced radio emissions visibility for various observation geometry (source location and observer location), and various emission pattern parameters (emission cone aperture, thickness, with possible variation with frequency). This model has been used to interpret Io-DAM radio emissions (Hess et al., 2008, 2010) as well as Saturn Kilometric Radiation (Lamy et al., 2008). We use here this tool to predict the occurrences of the HOM and DAM emissions, as seen from the orbits of the galilean satellites.

The visibility predictions shown here provide the envelope of the time–frequency domain in which the radio

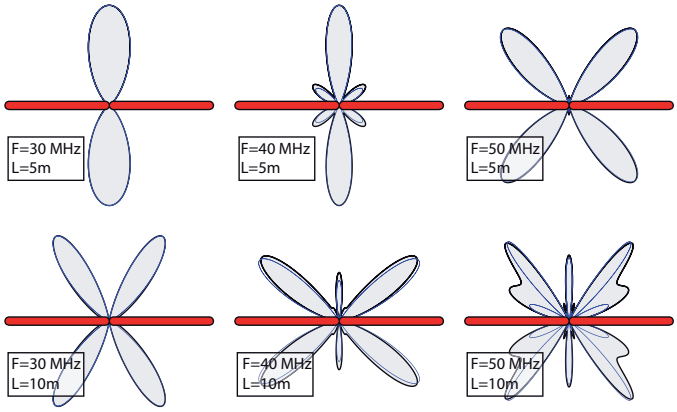

Figure 6: Electric dipole antenna beaming pattern for various lengths and central frequency. The thin blue line shows the beaming pattern at the given frequency, whereas the thick black line shows the beaming pattern for a 10 MHz band width centered on that frequency. The electric dipole is represented in red.

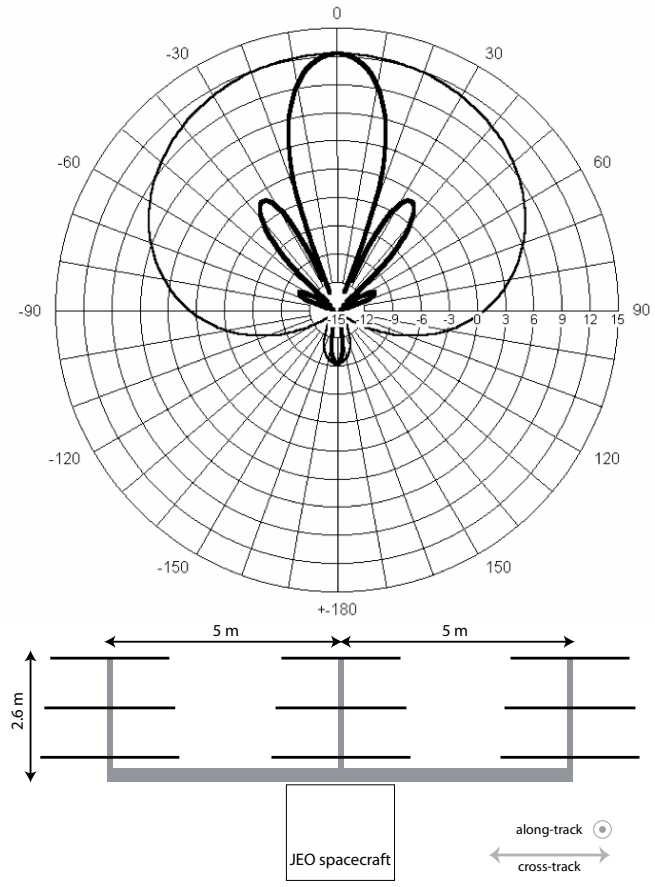

Figure 7: Yagi antenna (bottom) and its corresponding antenna diagram (top), for along-track (thin line) and cross-track (bold line). Figure adapted from Blankenship et al. (1999)

emissions may be observed from an observer at a given location. This does not mean that radio emission are always present in that domain. However, outside that domain, radio emissions are not visible. Hence, we can derive the shadow zones that are clean from radio emissions.

4.2. Radio Emissions Visibility

Fig. 8 shows auroral oval radio emissions (non-Io-DAM) as seen from the vicinity of each of the four Galilean satellites. The high frequency limit of the auroral oval radio emissions are drawn on these figures: dotted line for northern hemisphere and dashed line for southern hemisphere. The visibility of the radio emissions clearly depends on the longitude of the observer. The longitude system used here is the System III Longitude, hereafter referred to as λ_{III} (Higgins et al., 1997). For instance, at Europa, it is possible to observe northern and southern radio emissions up to 22 MHz, for all jovian longitudes, but above 22 MHz, there is a shadow zone between λ_{III}=300° and 330°. This shadow zone enlarges with higher frequencies: at 33 MHz, radio emissions are only visible from λ_{III}=60° to 240°. The jovian radio emissions are visible up to 42 MHz at around λ_{III}=150°. It is thus possible to predict shadow zones, in which the jovian auroral radio emissions are beamed out from the observed.

Supplementary Figs. S01, S02, S03 and S04 are movies of non-Io-DAM radio source locations as seen from an observer close to Io, Europa, Ganymede and Callisto, respectively. In each movies, the top panel shows the visible radio source locations as seen from the observer and the bottom panel shows the predicted dynamic spectrum. On that latter panel, the vertical cursor indicates the longitude of the observer, which is recalled at the top right of the figure. Each of the movies are covering one full rotation of Jupiter. They can be used for operation planning.

It is also possible to model and predict the visibility of Io controlled radio emissions. Fig. 9 shows Io-DAM emissions as seen from the distance of Ganymede's orbital radius. Note that this simulation does not take into account the orbital motion of Ganymede, that has must be included when computing the actual prediction the radio sources visibility for an observer orbiting Ganymede.

Supplementary Fig. S05 shows an example of Io-DAM emissions as seen from an observer orbiting Europa. The top-left panel show the visible radio source locations, as seen from the observer, the top-right panel shows the orbital configuration of Io and Europa around Jupiter at the time of the simulation, and the bottom panel shows the simulated dynamic spectrum of Io-DAM radio emissions. The vertical cursor on that latter panel corresponds to the data displayed on the two top panels.

Combining all these products, it is possible to model the various radio emissions visibility for a given spacecraft location, and thus predict the possibly actives time-frequency domain and the shadow zones, in which the radar will operate in a clean radio environment.

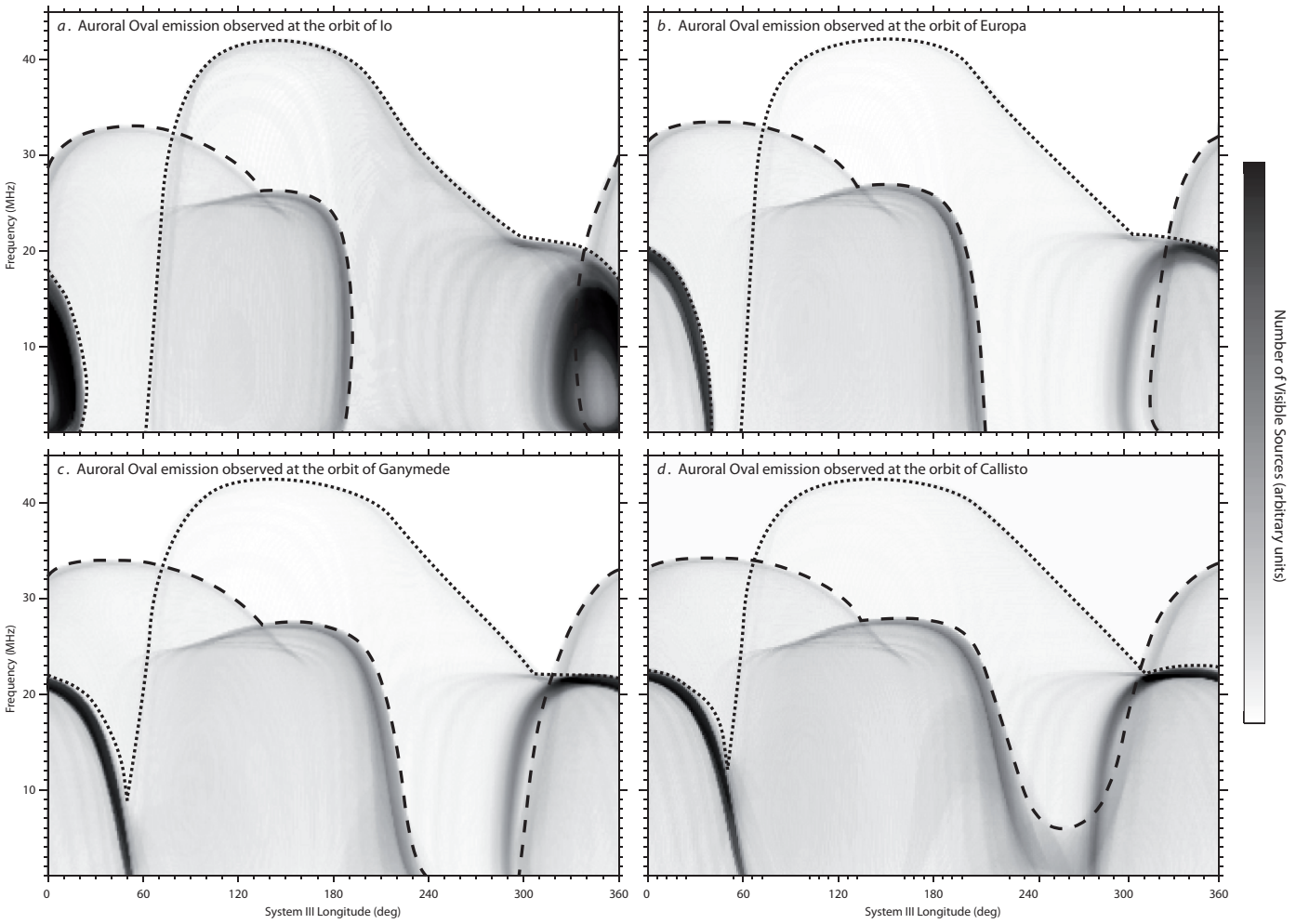

Figure 8: Simulation with ExPRES of the auroral oval (non-Io-DAM) radio emissions of Jupiter, as seen from the orbit of Io (panel *a*) , Europa (panel *b*), Ganymede (panel *c*) or Callisto (panel *d*), as a function of the jovian system III longitude (λ_{III}). The dashes (resp. dotted) line is the visibility envelope of the northern (resp. southern) auroral radio sources.

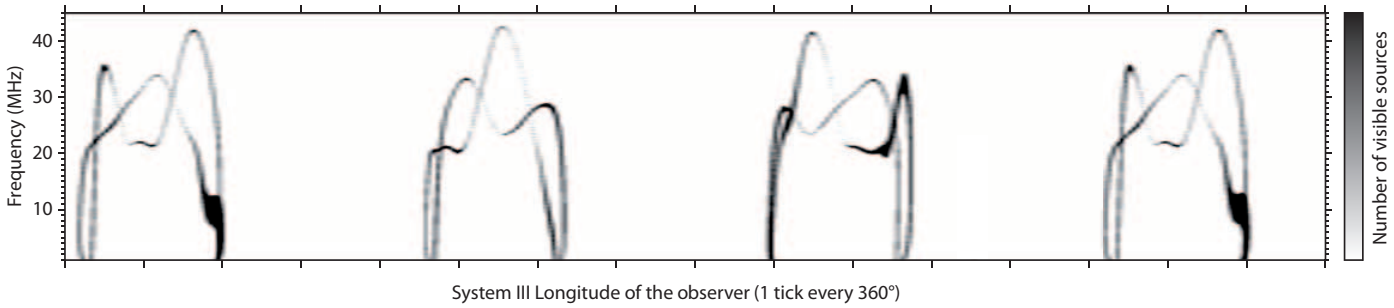

Figure 9: Simulation with ExPRES of the Io-DAM radio emissions of Jupiter, as seen from the distance of Ganymede's orbital radius as a function of the jovian system III longitude (λ_{III}). Northern and southern sources are both represented.

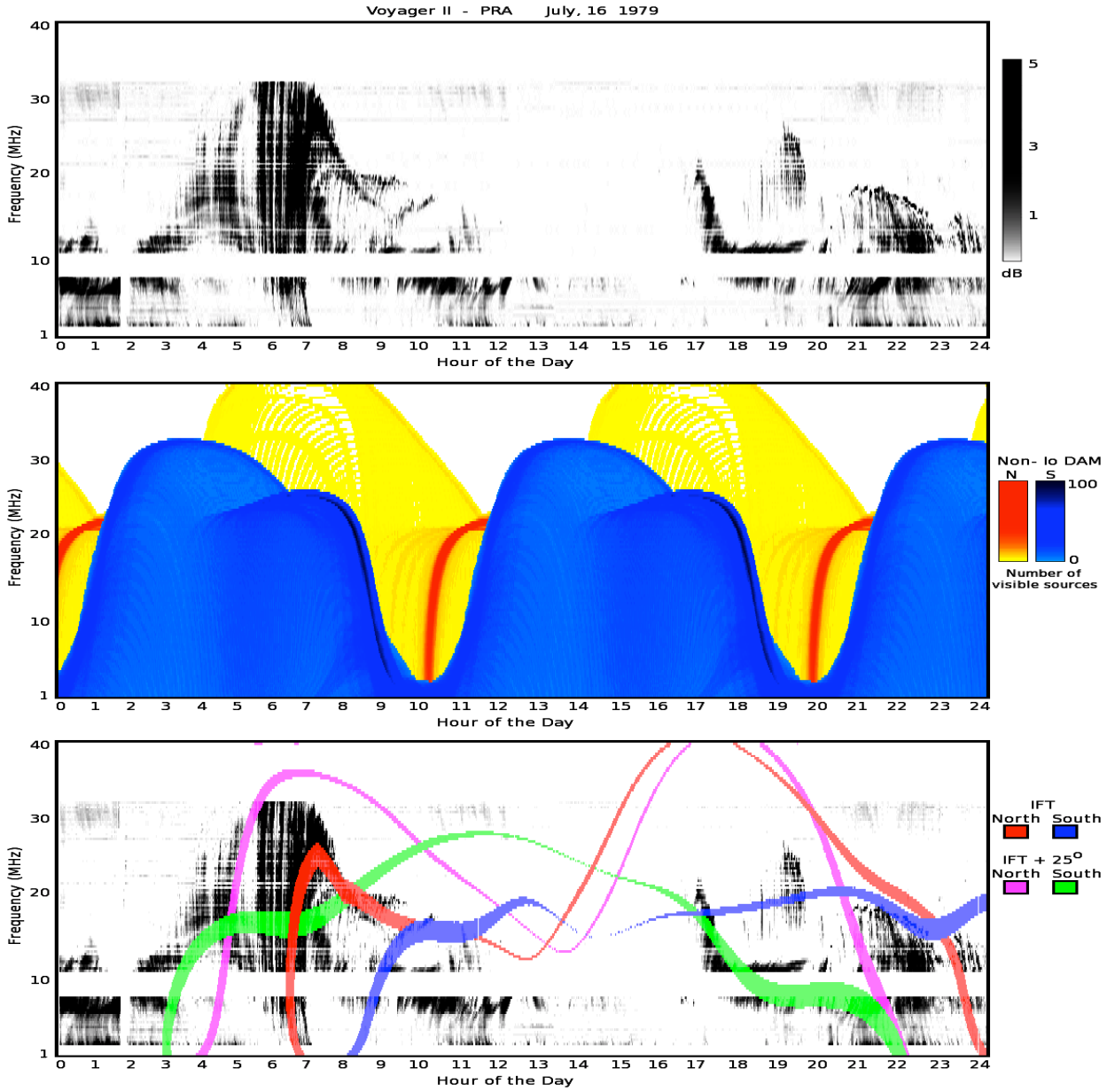

Figure 10: Voyager 2 radio data (top panel, same interval as on Fig. 3, with simulated auroral oval DAM emissions (middle panel) and Io-controlled DAM emission (bottom panel). Color code: for the middle panel, northern emissions are in red-yellow color code, southern ones in blue color code; for the bottom panel, radio emissions emitted on the Io flux tube (IFT) are in red and blue (for northern and southern sources, respectively), and radio emissions on magnetic fields lines shifted in longitude by 25° are also represented (pink for northern emissions, green for southern ones).

4.3. Back to Voyager data

In order to test the ExPRES tool, we modeled one day (July 16, 1979) of Voyager 2 (VG2) PRA data, using the new VIPAL magnetic field model (Hess et al., 2010). At this time, VG2 has been cruising from 84 to 96 R_J (1 R_J=71492 km), at a local time of ∼2.45 hours. This period of time was already studied by Goldstein and Thieman (1981) and Ray and Hess (2008). The analysis is presented on Fig. 10. The top panel shows the power spectral density (selected in right handed polarization) with respect to time (in hours of day) and frequency (MHz). The middle plot is the modeled dynamic spectrum for auroral oval DAM emissions (yellow-red and blue colors bars for northern and southern sources respectively). The bottom panel is the comparison between real data and Io-controlled DAM emissions.

We interpret the various emissions observed by Voyager as follows. The 0300-0900 (1 to 35 MHz) event is an Io-DAM emission from the northern hemisphere (Io-B emission): the red curve (bottom panel) is the modeled radio emission emitted on the Io flux tube (IFT), preceded by typical striated emissions covering the whole spectral range down to 25° ahead from the IFT (pink curve of bottom panel) (these trailing emissions are connected to the wake Io's auroral footprint). The 2100-2400 (5 to 18 MHz) event is an Io-DAM emissions from the southern hemisphere (Io-C emission): the blue curve (bottom panel) is the modeled radio emission emitted on the IFT, preceded by typical striated emissions. The 1700-1800 (10 to 20 MHz) event is a southern auroral (non-Io) DAM event, that compares well with the blue region (middle panel) at this time. The 1900-2000 (15 to 25 MHz) event is a northern auroral (non-Io) DAM event. Surprisingly, very faint radio emissions are visible around 30 MHz (0000-0200, 1000-1300 and 2100-2300). They are modulated at the rotation rate of Jupiter and may be related to electron precipitations at higher latitude than that of the main auroral oval. This will be the subject of an upcoming study.

4.4. Radio source occultation

Knowing the location of the visible radio sources, it is possible to compute the geometrical shadow zone produced by the observed galilean satellite itself. We study here the case of JGO orbiting Ganymede, during its final orbital phase: a circular orbit at an altitude of 200 km. A schematic view of the system is provided on Fig. 11. The extent of the satellite-shadowed orbital portion is displayed in green. This shadowed interval depend on the frequency and on jovian longitude λ_{III} as well as the Io location. These parameters are defining the location of the visible radio sources, as shown at the beginning of this section.

In order to compute the typical extent of the shadowed interval, we use the following parameters: the altitude of the radio source above the jovian equatorial plane is $h_N = h_S = 1.1\ R_J$, their distance to the rotation axis of Jupiter is $d_N = d_S = 0.2\ R_J$ (see panel (a) of Fig. 11). We thus get the angles α_1 and α_2 from the following equations: $\tan(\alpha_1) = (h_N - R_G)/(d_G - d_N)$ and $\tan(\alpha_2) = (h_S - R_G)/(d_G - d_S)$. We also define the radius of Ganymede's orbit as $d_G = 15.0\ R_J$, and its radius as $R_G = 5260$ km. We also recall that $1\ R_J = 71492$ km. In our simple case, these angle are equal: $\alpha_1 = \alpha_2 = 3.9°$. The angle β can is directly linked to the altitude of JGO's orbit as $\cos\beta = R_G/(R_G + z)$. With an orbital radius of 200 km, we get $\beta = 15.6°$. The angular extent δ of the shadowed orbital interval is thus simply $\delta = 180° - (\alpha_1 + \alpha_2 + 2\beta)$. Using the computed values of α_1, α_2, and β, we can get $\delta = 141.0°$, which corresponds to 39% of JGO's orbit around Ganymede. Using a 500 km orbit, we get $\delta = 124.1°$ (or 34% of JGO's orbit). This simple computation shows that the radio source occultation by the studied galilean satellite is permitting radar studies only during 35 to 40% of the orbit.

4.5. Further investigation steps

There are two ways of increasing the accuracy of the ExPRES visibility predictions: using a more accurate magnetic field model, and refining the radio source opening angle models. Both aspects can be improved.

For the present study, we used the VIPAL magnetic field model (Hess et al., 2010), which is an enhanced VIP4 (Connerney et al., 1998), using recent observations of the Io auroral footprint location. This new model is the only existing magnetic field model that can reproduce the northern radio emission shape in the time-frequency plots, using ExPRES. However, the ultimate magnetic field model for such studies will be provided by the JUNO mission, which will measure the magnetic field within the radio source regions. This magnetic field model should be available by 2018, two years before the EJSM mission is launched.

The second aspect that must be improved is the modeling of the opening angle of radio emission radiating pattern. Several datasets will have to be studied for that purpose (such as the Jupiter flyby of Cassini, Voyager data, or long term ground based observation) using the ExPRES tools or other analysis such as that used by Imai et al. (2008). These analyses will probably have to be refined after JUNO's magnetic field model, but a lot can already be done now. Although the Io controlled radio emissions are now well model, the auroral oval radio emission opening angle has only been measured up to 16 MHz with Cassini/RPWS (Radio and Plasma Waves Science) data. Higher frequency analysis implies the use of ground based measurements. Finally, as observed on the VG2 PRA data (see Figure 10), there are faint emissions around 30 MHz, which are modulated at the jovian sidereal period. These radio emissions are not yet interpreted or modeled.

5. Radio signal mitigation

In order to use radar instrumentation in the vicinity of Jupiter, radio signal mitigation solutions have to be studied if we want to operate when the observer is not in the

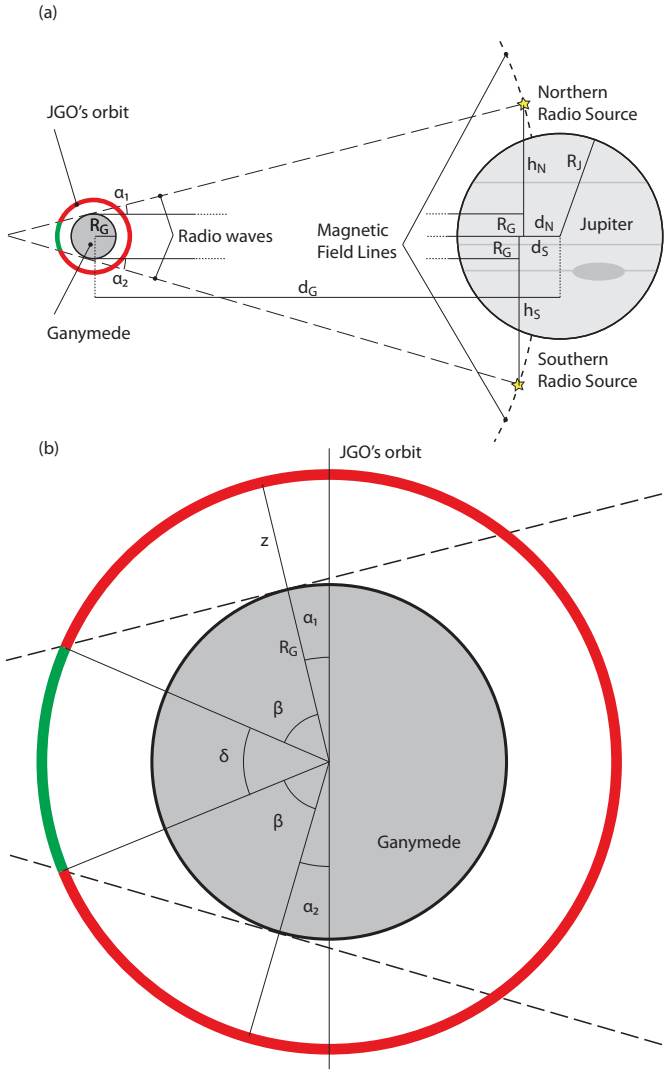

Figure 11: Schematic view of JGO final orbit phase around Ganymede, with radio sources close to Jupiter. Panel (a) shows a synoptic view of the whole system, with two visible radio sources, one in each hemisphere, emitted on high latitude magnetic field lines. Panel (b) is a close-up of the vicinity of Ganymede, with JGO's orbit and the various angles defined in the text.

satellite shadow with respect to Jovian radio sources. Various suggestions are presented here, including synergies with the RPW (Radio and Plasma Waves) instrumentation. This list is not exhaustive and other solutions may arise during the preparation of the EJSM mission.

5.1. Goniopolarimetric discrimination using solely the radar antenna

The auroral radio sources are very localized and almost fully polarized (either circularly or elliptically). With a 2 antenna receiving system, it may be possible to set up an onboard discrimination algorithm, based on source localization and polarization assumptions. If this is done within the radar receiver, it may have to take into account the various onboard processes applied to the radar echoes (such as the dedispersion stage). Such algorithms have to be developed using the goniopolarimetric equations (Cecconi and Zarka, 2005; Cecconi, 2010), but it may not be efficient enough.

5.2. Dipole antenna pattern nulling

The antenna used for radar science on JGO is an electric dipole antenna. The beaming pattern of such an antenna is recalled in Fig. 6. In that figure, the $\nu = 30MHz$ and $L = 5\,m$ case is representative of a short antenna diagram with a gain $G = 3/2$. The $\nu = 40MHz$ and $L = 5\,m$ case is representative of an adapted antenna with a gain $G \sim 3.3$, which is the best possible gain for an electric dipole. Other cases shows multiple main beams and, more problematically, nulls in the direction perpendicular to the antenna, where the observed object is usually placed. However, there is always a null in the antenna direction. This implies that placing Jupiter or its radio sources close to the antenna axis will considerably decrease the noise coming from Jupiter. This shall be studied carefully depending on the λ_{III} of the observer, and on the final orbital characteristics. If such orbital and spacecraft attitude configurations are possible to plan, it would add some new science windows for radar teams.

As the expected noise coming from Jupiter is as high as 50 dB above the galactic background, realistic antenna modeling is required, in order to prove that a strong enough attenuation can be achieved. Such a study will have to be conducted after the spacecraft designs have been selected by ESA and NASA. Efficient antenna response simulations can be done using the method of moments simulating the distribution of currents on the spacecraft and antennas (Harrington, 1968; Oswald et al., 2007).

The beaming pattern shape of the Yagi antenna chosen for JEO implies much better rejection of interferences coming opposite to the observing direction (see Fig. 7). However, the beam is only narrow on the cross-track direction, interferences emitted by sources located in the along-track direction are attenuated by 12 dB, which is not enough for attenuating radio emissions that can be 50 dB above background. However, if the JEO instrument operates at

50 MHZ, as planned, there is no natural interferences problem.

5.3. Instrumental Synergies

Finally, it is possible to propose instrumental synergies with the high frequency radio receiver included in the RPW instrument. Note that RPW instrumentation is only planned on JGO, at the time of writing.

First, if the RPW can operate during radar sensing, the radio receiver will be able to observe the radar echoes. Thanks to its three antennas and goniopolarimetric capabilities, the radio receiver will be able to measure the mean direction of arrival, polarization, flux and apparent source size of the radar echoes. As the echoes are randomly polarized, they can easily be discriminated from jovian radio emissions that are fully polarized. However, if a linear polarization component remains in the radar echoes, the goniopolarimetric techniques will provide erroneous results, leading to possible false alarm detection.

In order to efficiently discriminate between radar signals from faint jovian radio emissions, it is necessary to look at the frequency context during the radar sequence. The jovian radio emissions are indeed either vertically or arc-shape structured in this frequency range (see e.g., Figs. 3 and 10). A good test would be to check if radio emissions are present at higher and lower frequencies (outside the operating radar bandwidth), then that particular time interval is most likely polluted with jovian radio noise. This could be done with high rate data sampling on a limited set of frequencies. Onboard processing may also be put together for onboard data mitigation. This would imply real-time onboard communication between the radar and the RPW instruments.

6. Discussion

We presented the natural radio sources in the environment of Jupiter. These natural radio emissions are very intense non thermal radio emissions that are well above ($\sim$ 50 dB) above the galactic background below their high frequency cutoff at $\sim$ 40 MHz. These radio emissions are strongly beamed along a thin hollow cone that can be modeled. It is thus possible to predict the visibility of these radio emissions for a given observing geometry.

The visibility modeling indicates favorable configurations below 40 MHz, down to $\sim$22 MHz, depending on the longitude of the observer and on that of Io. Below 22 MHz, radio sources may always be visible. Indeed, we predict the visibility of the radio emission, not there occurrence. This means that their temporal occurrence are not modeled, but the time-frequency domain envelope, in which they can occur. The visibility analysis hence provides us the shadow zones, that are clean from jovian radio emissions. The visibility modeling of Io related radio (Io-DAM) sources has been thoroughly checked in several previously studies. It is not the case for auroral oval radio emissions (non-Io-DAM), for which we used the same emission beam opening angle model than that of Io-DAM. The results of the reanalysis of Voyager data indicates that this assumption was legitimate. However, further work on available datasets needs to be done to improve the modeling of non-Io-DAM visibility. The results of the JUNO mission will improve our knowledge of the Jovian magnetic field in the radio sources region (which is essential for more accurate radio source modeling). JUNO will also put definitive numbers on the high frequency cutoff of DAM emissions. Even if JUNO will not have goniopolarimetric capabilities, it will put constraints on the radio source properties such as their location and their emission beam topology.

The visibility modeling shows that the visible radio sources are located between 0 and 0.5 R_J above the Jovian limb, close to the magnetic poles of the planet. The equatorial extension of the radio sources location is typically ± 0.5 R_J centered on the rotation axis of Jupiter.

When the emission is visible, the safest strategy is to operate in the far side of Galilean satellite. This reduces the orbital fraction available for radar studies to $\sim 35\%$. However, strategies have been proposed to mitigate the natural radio emissions of Jupiter: goniopolarimetric analysis, antenna nulling, or frequency context observations. That latter proposition can be applied on the JGO spacecraft which includes an RPW instrument in the core payload, whereas the JEO spacecraft don't. We thus promote a reduced RPW instrumentation onboard JEO, that would provide this frequency context observations, in addition to the RPW science objectives. Considering the antenna pattern nulling, the precise location of the radio sources has to be taken into account. These sources may be far from Jupiter: the lower frequency, the farther from Jupiter, above the magnetic poles.

Systematic operational visibility plots will be computed in cooperation with radar teams. A website containing up-to-date visibility simulations, as well as online tools to compute other radio source visibility products, is in preparation and will be available at the following URL: `http://www.lesia.obspm.fr/ExPRES`

7. Conclusion

We have presented the natural radio emission emitted by the Jovian magnetosphere, concentrating on the auroral radio emissions, that can be considered as noise for radar studies below 40 MHz. We have shown that it is possible to predict which system III longitudes are cleaned from radio emissions above 22 MHz, whereas there can be radio emissions at all times below that frequency. We proposed mitigation solutions to discriminate or attenuate the Jovian radio emissions. We strongly support instrumental synergies, especially with RPW instrumentation, on both EJSM spacecraft.

Quantity		Unit
Operating frequency	ν	Hz
Operating wavelength	λ	m
Speed of light	c	m/s
Antenna effective area	A_{eff}	m^2
Antenna main lobe solid angle	Ω_A	sr
Antenna gain	G	–
Spectral Power Density	$P(\nu)$	W/Hz
Spectral Flux Density	$S(\nu)$	$W/m^2/Hz$
Brightness density	$B(\nu)$	$W/m^2/Hz/sr$
Brightness temperature	T_B	K
Antenna Temperature	T_A	K
Source solid angle	ω_s	sr

Table A.3: Quantities and units useful for radio data analysis.

Acknowledgments

This work has been conducted at the occasion of the EJSM assessment studies. The authors thank the members of the EJSM Electromagnetic Sensors Study, the EJSM/JGO/SSR (Sub-Surface Radar) and the EJSM/JEO/IPR (Ice Penetrating Radar) teams, for helpful and fruitful discussions. BC and SH also thank L. Ray and N. André for helpful discussions and comments. The French authors thanks CNRS (Centre National de la Recherche Scientifique) and CNES (Centre National d'Etudes Spatiales) for supporting EJSM studies.

Appendix A. On Radio Measurements

Several quantities (measured in various units) are used to characterize the strength of a electromagnetic radio wave. These quantities and their units are presented in Table A.3. We provide here operational conversion tools in the case of a dipole antenna.

A.1. Effective area, Main lobe and antenna Gain

One of the key characteristics of an antenna is the shape of its main lobe. The solid angle of the main lobe is defined by the set of directions in space where the gain of the antenna is larger than half of its maximum gain. The solid angle of the main lobe is simply called the main lobe.

The main lobe of an antenna is related to the antenna effective area by :

$$A_{eff}\Omega_A = \lambda^2 \tag{A.1}$$

The main lobe of a short dipole is:

$$\Omega_A = 8\pi/3\, sr. \tag{A.2}$$

The effective area of a short dipole antenna is thus:

$$A_{eff} = \frac{3\lambda^2}{8\pi} \tag{A.3}$$

Although a dipole antenna is a thin linear conductor, it has an effective area, which can be regarded as its "radio cross-section".

The antenna gain is defined as:

$$G = 4\pi/\Omega_A. \tag{A.4}$$

For a short dipole, we get $G = 3/2$.

A.2. Spectral power density, Spectral flux density

The spectral power density is the power received by the antenna, per unit of frequency. The spectral flux density is the received power per unit of surface and of frequency. Hence, spectral power density and Spectral flux density are linked by the following relationship:

$$S(\nu) = P(\nu)/A_{eff} \tag{A.5}$$

A.3. Brightness density and temperature of the source

The Brightness density is the power sent by the source per unit of surface, frequency and solid angle. The Rayleigh-Jeans law links the brightness density and the brightness temperature:

$$B(\nu) = \frac{2k_B T_B}{\lambda^2} \tag{A.6}$$

A.4. Antenna temperature

The Antenna temperature T_A is related to the Brightness temperature T_B by the following relationship:

$$T_A\Omega_A = T_B\omega_s \tag{A.7}$$

where ω_s is the source solid angle as viewed from the spacecraft. This equation implies that $\omega_s < \Omega_A$. When this condition is not verified, i.e. when $\omega_s \geq \Omega_A$, we assume $\omega_s = \Omega_A$. This simply reflects that the antenna cannot see out of its antenna pattern. Hence, in that case, we have $T_A = T_B$. Equation A.7 also implies that the antenna pattern is pointed to the center of the source.

In case of a point source, ω_s is unknown and T_B cannot be defined. In this case, we can only measure T_A.

A.5. Effect observing geometry

When the source is not at the center of the main lobe, a geometrical correction factor σ_g have to be introduced in order to interpret the measured antenna temperature, spectral flux density or spectral power density. This factor characterized the fraction of the signal that is observed by the receiving system, and depends on the shape of the main lobe, and on the direction of the wave vector with respect to the antenna direction. In case of a point source observed with a perfect short dipole, we have $\sigma_g = \sin^2\theta$, where θ is the angle between the direction of the wave vector and that of antenna.

A.6. Effect of the wave polarization

A radio antenna is sensitive to only one polarization direction or sense (in case of linear or circular polarization, respectively). An antenna polarization factor σ_p can be introduced and characterize the fraction of the signal that is observed by the receiver by the instrumental polarization selection. The value of σ_p depends on the polarization properties of the antenna and that of the observed radio wave:

- Circularly polarized wave observed with a linear dipole antenna: Half of the incident power is sensed, hence $\sigma_p = 1/2$;
- Unpolarized wave observed with any antenna: Half of the incident power is sensed, hence $\sigma_p = 1/2$;
- Linearly polarized wave observed with a linear dipole antenna: The power fraction caught by the antenna depends on the angle ψ between the axis of linear polarization of the wave, and that of the antenna, hence, $\sigma_p = \cos^2 \psi$. Hence, if the wave linear polarization axis is aligned with the antenna direction (i.e. $\psi = 0$), we get $\sigma_p = 1$.
- In general, real radio signals are composed of an unpolarized part and a polarized part that can be either linearly, elliptically or circularly polarized. Hence, σ_p takes any values in the range $[0, 1]$.

References

B. Burke, K. Franklin, Observations of a variable radio source associated with the planet jupiter, J. Geophys. Res. 60 (1955) 213.

P. Zarka, Auroral radio emissions at the outer planets: Observations and theories, J. Geophys. Res. 103 (1998) 20159–20194.

H. Cane, Spectra of the non-thermal radio radiation from the galactic polar regions, Mon. Not. R. astr. Soc. 189 (1979) 465–478.

P. Zarka, The auroral radio emissions from planetary magnetospheres: What do we know, what don't we know, what do we learn from them?, Adv. Space. Res. 12 (1992) 99–115.

P. Zarka, B. Cecconi, W. Kurth, Jupiter's low-frequency radio spectrum from Cassini/Radio and Plasma Wave Science (RPWS) absolute flux density measurements, J. Geophys. Res. 109 (2004) A09S15.

P. Zarka, Plasma interactions of exoplanets with their parent star and associated radio emissions, Planet. Space Sci. 55 (2007) 598–617.

C. Wu, L. Lee, A theory of the terrestrial kilometric radiation, Astrophys. J. 230 (1979) 621–626.

R. Treumann, The electron-cyclotron maser for astrophysical application, Astron. Astrophys. Rev. 13 (2006) 229–315.

A. Lecacheux, Polarization aspects from planetary radio emissions, in: H. Rucker, S. Bauer, B.-M. Pedersen (Eds.), Planetary Radio Emissions II, Austrian Acad. Sci. Press, Graz, Austria, 1988, pp. 299–314.

A. Lecacheux, A. Boischot, M. Boudjada, G. Dulk, Spectra and complete polarization state of two, Io-related, radio storms from Jupiter, Astron. Astrophys. 251 (1991) 339–348.

M. Reiner, M. Desch, M. Kaiser, R. Manning, J. Fainberg, R. Stone, Elliptically polarized bursty radio emissions from Jupiter, Geophys. Res. Lett. 22 (1995) 345–348.

G. Ellis, Observations of the Jupiter S-bursts between 3.2 and 32 MHz, Aust. J. Phys. 35 (1982) 165–175.

J. Queinnec, P. Zarka, Io-controlled decameter arcs and Io-Jupiter interaction, J. Geophys. Res. 103 (1998) 26649–26666.

S. Hess, B. Cecconi, P. Zarka, Modeling of Io-Jupiter Decameter Arcs, Emission Beaming and Energy Source, Geophys. Res. Lett. 35 (2008).

L. Ray, S. Hess, Modeling the Io-related DAM emissions by modifying the beaming angle, J. Geophys. Res. 113 (2008) A11218.

M. Imai, K. Imai, C. Higgins, J. Thieman, Angular beaming model of Jupiter's decametric radio emissions based on Cassini RPWS data analysis, Geophys. Res. Lett. 35 (2008) L17103.

V. Ryabov, B. Ryabov, D. Vavriv, P. Zarka, R. Kozhin, V. Vinogradov, V. Shevchenko, Jupiter S-bursts: Narrow-band origin of microsecond subpulses, J. Geophys. Res. 112 (2007).

P. Zarka, T. Farges, B. Ryabov, M. Abada-Simon, L. Denis, A scenario for jovian S-bursts, Geophys. Res. Lett. (1996) 125–128.

L. Lanzerotti, K. Rinnert, G. Dehmel, F. Gliem, E. Krider, M. Uman, J. Bach, Radio frequency signals in Jupiter's atmosphere, Science 272 (1996) 858–860.

A. Cook II, T. Duxbury, G. Hunt, First results on Jovian lightning, Nature 280 (1979) 794.

D. Gurnett, R. Shaw, R. Anderson, W. Kurth, Whistlers observed by Voyager 1 - Detection of lightning on Jupiter, Geophys. Res. Lett. 6 (1979) 511–514.

M. Desch, W. Borucki, C. Russell, A. Bar-Nun, Progress in planetary lightning, Reports on Progress in Physics 65 (2002) 955–997.

P. Zarka, W. Farrell, M. Kaiser, E. Blanc, W. Kurth, Study of solar system planetary lightning with LOFAR, Planet. Space Sci. 52 (2004) 1435–1447.

P. Zarka, On detection of radio bursts associated with Jovian and Saturnian lightning, Astron. Astrophys. 146 (1985) L15–L18.

W. Farrell, M. Kaiser, M. Desch, A model of the lightning discharge at Jupiter, Geophys. Res. Lett. 26 (1999) 2601–2604.

D. Sentman, E. Wescott, D. Osborne, D. Hampton, M. Heavner, Preliminary results of the sprites 94 aircraft campaign: red sprites, Geophys. Res. Lett. 22 (1995) 1205–1208.

X. Bonnin, Etude stéréoscopique de la directivité des sursauts radio solaires de type III aux fréquences inférieures à 10 MHz., Ph.D. thesis, Université Paris Diderot - Ecole Doctorale d'Astronomie et d'Astrophysique d'Ile-de-France, 2008.

R. R. Weber, Low frequency spectra of type III solar radio bursts, Sol. Phys. 59 (1978) 377–385.

I. de Pater, LOFAR and Jupiter's radio (synchrotron) emissions, Planet. Space Sci. 52 (2004) 1446–1454.

I. de Pater, D. Dunn, VLA observations of Jupiter's synchrotron radiation at 15 and 22 GHz, Icarus 163 (2003) 449–455.

D. Santos-Costa, S. Bolton, Discussing the processes constraining the Jovian synchrotron radio emission's features, Planet. Space Sci. 56 (2008) 326–245.

D. Santos-Costa, Modélisation des Ceintures de Radiations d'Electrons de Jupiter Internes à Io, Ph.D. thesis, ENSAE, Toulouse, France, 2001.

J. Novaco, L. Brown, Nonthermal galactic emission below 10 MHz, Astrophys. J. 221 (1978) 114–123.

G. Dulk, W. Erickson, R. Manning, J.-L. Bougeret, Calibration of low-frequency radio telescopes using the galactic background radiation, Astrophys. J. 365 (2001) 294–300.

R. Manning, G. Dulk, The Galactic background radiation from 0.2 to 13.8 MHz, Astrophys. J. 372 (2001) 663–666.

W. Kofman, R. Orosei, E. Pettinelli, Radar Signal Propagation and Detection Through Ice, Space Sci. Rev. (2010).

P. Djurík, S. Kay, Parameter Estimation of Chirp Signals, in: Speech and Signal Processing, volume 38 of *IEEE Transactions on Acoustics*, pp. 2118–2126.

G. Picardi, S. Sorge, R. Seu, J. Plaut, W. Johnson, R. Jordan, D. Gurnett, R. Orosei, L. Borgarelli, G. Braconi, C. Zelli, E. Zampolini, The Mars Advanced Radar for Subsurface and Ionosphere Sounding (MARSIS): concept and performance, volume 5 of *IGARSS Proceedings*, IEEE, pp. 2674–2677.

G. Picardi, D. Biccari, R. Seu, J. Plaut, W. Johnson, R. Jordan, A. Safaeinili, D. Gurnett, R. Huff, R. Orosei, O. Bombaci, D. Calabrese, E. Zampolini, MARSIS: Mars Advanced Radar for Sub-

surface and Ionosphere Sounding, SP-1240, ESA Publications Division, ESTEC, Noordwijk, The Netherlands.

R. Seu, D. Biccari, R. Orosei, L. Lorenzoni, R. Phillips, L. Marinangeli, G. Picardi, A. Masdea, E. Zampolini, SHARAD: The MRO 2005 shallow radar, Planet. Space Sci. 52 (2004) 157–166.

D. Blankenship, B. Edwards, Y. Kim, P. Geissler, D. Gurnett, W. Johnson, W. Kofman, J. Moore, D. Morse, R. Pappalardo, G. Picardi, R. Raney, E. Rodriguez, X.-M. Shao, J. Weertman, H. Zebker, J. van Zyl, Feasibility study and design concept for an orbiting ice-penetrating radar sounder to characterize the three-dimensional distribution of subsurface water on Europa, Technical Report, 1999.

S. Hess, A. Pétin, P. Zarka, B. Cecconi, Modeling the Io-controlled Radio Arcs: Lead Angle and Particle Velocity Measurement, Planet. Space Sci. in press (2010).

L. Lamy, P. Zarka, B. Cecconi, S. Hess, R. Prangé, Modeling of Saturn Kilometric Radiation arcs and equatorial shadow zone, J. Geophys. Res. 113 (2008).

C. Higgins, T. Carr, F. Reyes, W. Greenman, G. Lebo, A redefinition of Jupiter's rotation period, J. Geophys. Res. 102 (1997) 22033–22041.

S. Hess, B. Bonfond, P. Zarka, D. Grodent, Model of the Jovian magnetic field topology constrained by the Io auroral emissions, J. Geophys. Res. submitted (2010).

M. Goldstein, J. Thieman, The formation of arcs in the dynamic spectra of Jovian decameter bursts, J. Geophys. Res. 86 (1981) 8569–8578.

J. Connerney, M. Acu.na, N. Ness, T. Satoh, New models of Jupiter's magnetic field constrained by the Io flux tube footprint, J. Geophys. Res. 103 (1998) 11929–11939.

B. Cecconi, P. Zarka, Direction finding and antenna calibration through analytical inversion of radio measurements performed using a system of 2 or 3 electric dipole antennas, Radio Sci. 40 (2005) RS3003.

B. Cecconi, Goniopolarimetric techniques for low-frequency radio astronomy in space, in: M. Huber, A. Pauluhn, J. Timothy (Eds.), Observing Photons in Space, volume 9 of *ISSI Scientific Reports Series*, Springer, 2010, pp. 263–277.

R. Harrington, Field Computation by Moment Methods, Krieger, R.E., 1968.

T. Oswald, W. Macher, H. Rucker, G. Fischer, U. Taubenschuss, J.-L. Bougeret, A. Lecacheux, M. Kaiser, K. Goetz, Various methods of calibration of the STEREO/Waves antennas, Adv. Space. Res. (2007) submitted.